CFD Verification and Validation of Added Resistance and Seakeeping Response in Regular Oblique Waves

MARINE 2021

Henrik Mikkelsen[1,*], Yanlin Shao[1] and Jens H. Walther[2]

[1] Technical University of Denmark (DTU)
Department of Mechanical Engineering
Nils Koppels Allé, Building 404, 2700 Kgs. Lyngby, Denmark.

[2] Swiss Federal Institute of Technology Zurich (ETH Zrich)
Computational Science & Engineering Laboratory
Clausiusstrasse 33, CH-8092 Switzerland

[*] Corresponding author: Henrik Mikkelsen, hmik@mek.dtu.dk

ABSTRACT

The importance of CFD is increasing in marine hydrodynamics in studying seakeeping and added resistance of ships. While extensive numerical studies have been reported for various ships in head seas in the literature, much fewer CFD studies are found for oblique waves, which in practice is very important in, for instance, estimating required power and manoeuvrability of ships in realistic sea states. In this paper, the added resistance and motion responses for the KCS container ship in regular waves are studied and validated systematically for five wave headings and six wavelengths using CFD. The ship is free to heave, pitch, and roll. Implementations to the commercial CFD code are made to fix the yaw and surge motions. Extensive verification of the CFD model finds the estimated spatial and temporal discretization errors to be less than 5 %. Results of the verified CFD model are compared with up to three sets of experimental data sets, Potential Flow (PF) and existing CFD results from the literature. In general, the present CFD results show significantly better agreement with the experiments than previously published CFD results. The agreement between the present CFD model and experiments is better for the headings, where the uncertainties of the experiments are smallest. Present CFD results confirm previous published numerical findings that the experimental roll motion is excessive for the 45 ° heading.

Keywords: CFD; Added resistance in waves; Oblique waves; Validation.

NOMENCLATURE

a_k, b_k	Fourier coefficients [-]	$f_{Z\theta}$	Natural heave/pitch frequency without forward speed [Hz]
A	Wave amplitude [m]	$f_{Z\theta,U}$	Natural heave/pitch frequency with forward speed [Hz]
A_k	k-th amplitude [m] or [°] or [N]	f_e	Encounter frequency [s^{-1}]
B	Beam [m]	k	Turbulent kinetic energy [$m^2\,s^{-2}$]
C_μ	Empirical constant [-]	k	Wavenumber [m^{-1}]
e_a	Approximate relative error [-]	k_{xx}	Longitudinal radius of gyration [m]
e_{ext}	Extrapolated relative error [-]	k_{yy}	Transverse radius of gyration[m]
f_i	Body force [$kg\,m^{-2}s^{-2}$]	KG	Vertical center of gravity (from keel) [m]
f_e	Encounter frequency [Hz]	L_{pp}	Length between perpendiculars [m]
f_ϕ	Natural roll frequency without forward speed [Hz]	p	Pressure [Pa]
$f_{\phi,U}$	Natural roll frequency with forward speed [Hz]		

p	Apparent order of convergence [-]
r	Refinement ratio [-]
R	Resistance [N]
R_0	Mean resistance [N]
R_{CW}	Calm water resistance [N]
s	Solution
s	Sign indicator
S_{ij}	Mean shear rate [s^{-1}]
T	Draft [m]
t	Time [s]
T_e	Encounter period [s]
$\mathbf{u}$	Velocity vector [$m\,s^{-1}$,$m\,s^{-1}$,$m\,s^{-1}$]
$\mathbf{u'}$	Turbulent fluctuating part of the velocity vector [$m\,s^{-1}$,$m\,s^{-1}$,$m\,s^{-1}$]
U	Speed [m/s]
y^+	Non-dimensional wall distance [-]
Z	Heave [m]
Z_1	First heave amplitude [m]
α	Volume fraction [-]
Δ	Displacement [kg]
ϵ	Turbulent dissipation rate [$m^2\,s^{-3}$]
ϵ	Relative error [m] or [°] or [N]
θ	Pitch [°]
θ_1	First pitch amplitude [°]
λ	Wave length [m]
μ	Dynamic viscosity [Pa s]
μ_a	Dynamic viscosity of air phase [Pa s]
μ_w	Dynamic viscosity of water phase [Pa s]
μ_t	Turbulent viscosity [Pa s]
ρ	Density [kg m^{-3}]
ρ_a	Density of air phase [kg m^{-3}]
ρ_w	Density of water phase [kg m^{-3}]
σ_{aw}	Added resistance [N]
τ_x	Skin friction in the x-direction [Pa]
ϕ	Roll [°]
ϕ_1	First roll amplitude [°]
ϕ_k	Solution on the k-th mesh [m] or [°] or [N]
ω_k	Angular frequency [$rad\,s^{-1}$]

CFD	Computational Fluid Dynamics
COG	Center of Gravity
DTC	Duisburg Test Case
DFBI	Dynamic Fluid Body Interaction
EFD	Experimental Fluid Dynamics
GCI	Grid Convergence Index
HOBEM	Higher Order Boundary Element Method
IIHR	Iowa Institute of Hydraulic Research
KCS	KRISO Container Ship
KVLCC2	KRISO Very Large Crude Carrier
PF	Potential Flow
STF	Salvesen-Tuck-Faltinsen
URANS	Unsteady Reynolds Averaged Navier-Stokes
UZ	University of Zagreb
VOF	Volume Of Fluid

1 INTRODUCTION

For the last decades most commercial ship hulls have been designed and optimized for sailing fully loaded with full speed in calm water. Traditionally, the effects of wind and waves have been included by adding a sea margin of 15 percent (Molland et al., 2011) to the required engine power. Over the last 10 years, this single design point approach has started to change by including more draughts and speeds into the design matrix (Psaraftis and Kontovas, 2014). This has narrowed the gap between the conditions ships are design for and the conditions the ships will operate in. However, almost all ship hulls are still designed using a combination of experience, towing tank tests and Computational Fluid Dynamics (CFD), mostly in calm water. The next natural step is to include the influence of interaction with waves into the ship hull design phase. Since almost no ships are constantly sailing in calm water, optimizing the ship hull to realistic sea states in the future has significant potential to reduce fuel costs and emissions. Seakeeping tests of motion responses and added resistance in towing tanks can be expensive, time demanding and dependent on the availability of the tanks. If numerical approaches are verified and validated to become trustworthy, they could be used with confidence in the design phase of new ship hulls. Since numerical simulations only require an available computer and not a large manufactured wooden ship model or a free towing tank slot, ship designers can easily test the seakeeping capabilities of tens or hundreds of ship hulls in the design phase. The use of numerical approaches also makes it possible to study the full-scale ship (Mikkelsen and Walther, 2020; Niklas and Pruszko, 2019; Jasak et al., 2018) and thereby avoiding scale effects. The knowledge of a ship's seakeeping properties is also important for both a comfort and safely point of view. Most often, the comfort limit is reached before the motion limit for safety, especially for passenger ships. For

non-passenger ships, comfort limits related to ship motions in waves are not as strict. For these ships, the safety can sometimes be the limiting factor, e.g., for container ships, where containers can fall into the sea, if motions become too large. However, the added resistance in waves are important for all ships, since the added resistance increases fuel consumption and potentially limits the ship speed.

One of the first studies of added resistance in waves is by Storm-Tejsen et al. (1973), who conducted added resistance experiments of the series 60 ships. Fujii and Takahashi (1975) compared experiments and strip theory simulations on the S175 container ship. Most seakeeping and added resistance research has been focusing on head waves. Added resistance in head waves using CFD, has been studied intensively by e.g. Sadat-Hosseini et al. (2013), who numerically studied the KRISO Very Large Crude Carrier (KVLCC2). Kim et al. (2017b) have also studied the KVLCC2 both using CFD and 3D potential flow theory. Park et al. (2016) studied the added resistance of a tanker in head waves at different drafts using the Salvesen-Tuck-Faltinsen (STF) strip theory (Salvesen et al., 1970) and a B-spline based time-domain Rankine panel method (Kim et al., 2011). Simonsen et al. (2013) and Wu et al. (2020) studied the added resistance of the KRISO Container Ship (KCS) in head waves both experimentally and using CFD.

Fewer validation studies have been conducted in oblique waves. Studying the ship-wave interaction in oblique waves is important in order quantify the added power and maneuverability in a realistic sea, where the waves are seldomly uni-directional. Fujii and Takahashi (1975) experimentally studied the added resistance on the S175 container ship in various headings relative to the incident wave. More resently, experimental studies of the Duisburg Test Case (DTC) and the KVLCC2 were conducted by Sprenger et al. (2016).

Valanto and Hong (2015) experimentally tested the added resistance of a confidential cruise ship in seven different headings identifying the 45 ° heading to give maximum added resistance. Park et al. (2019) investigated the added resistance of a confidential tanker both experimentally and numerically in oblique waves. Both strip theory and a 3D Rankine panel method were used and the 3D Rankine panel method predicted the motion in oblique waves with fair agreement. The accuracy of the 3D Rankine panel method was found to be low in predicting the added resistance. The strip method was overestimating the added resistance significantly. A study by Liu and Papanikolaou (2016) predicted the added resistance in oblique waves with a far-field method using Kochin function for a bulk carrier and the Duisburg Test Case (DTC) container ship with fair agreement with the experiments. In general the agreement between numerical results and experiments were better for the longer waves than the shorter waves. Yang et al. (2019) used a frequency-domain hybrid Higher Order Boundary Element Method (HOBEM) to predict the motion responses and added resistance of different ship types sailing in head and oblique waves. In general, good agreement between numerical and experimental results were found. Liu et al. (2018) studied the wave forces and motions of the DTC ship in oblique waves for a single short wave length. They found that the diffraction and radiation effects have significant influence on the non-linearity of wave forces. Gong et al. (2020) numerically studied added resistance and seakeeping performance of trimarans in oblique waves. The results showed that the variational trends of the added resistance and motion amplitudes of the trimaran in waves are significantly affected by the wave steepness and wave incident angles, which are also different from those of traditional mono-hull ships. Chuang and Steen (2013) studied the speed loss of a vessel sailing in oblique waves both numerically and experimentally. They found that the speed reduction due to added resistance and due to steering are at almost the same level for head sea and bow sea conditions for the studied tanker with twin azimuth propulsors. Uharek and Cura-Hochbaum (2018) studied the influence of inertial effects on the mean forces and moments on a twin screw passenger ship sailing in oblique waves using CFD. They found it important to either add inertial contributions to the numerical computations when comparing to experiments or to precisely determine the motions during the model tests and subtract these effects from the measurements. Mousavi et al. (2020) studied the motion responses in two oblique irregular wave headings using both CFD and a strip theory. Jin et al. (2017) experimentally and numerically studied the wave induced loads and motions on two gas carriers in a regular head wave and an oblique wave, both at zero forward speed. The study found that wave diffraction around the

ship becomes less profound and the water depth starts to influence the wave loads and ship motions, when increasing the wave length. The added resistance and motions responses of the S175 container ship in multiple wave headings were studied numerically by Kim et al. (2017a). Both 2D and 3D potential-flow methods were used for all headings and CFD was used for head and following seas. The study predicted the sea margin in head sea to be 17.2 %.

The study by Sadat-Hosseini et al. (2015) presented experiments, potential flow, and CFD computations for added resistance for variable headings and wave lengths for the KCS. They found that potential-flow method captures the heave and pitch motions well. However, surge, roll, and added resistance were not well predicted for most cases. The accuracy of the CFD calculations were better, but were only conducted for the single wavelength studied at the Tokyo 2015 CFD workshop (Hino et al., 2020). The Tokyo 2015 CFD workshop had a test case, where participants could submit CFD results of motion responses and added resistance for 5 headings and a single wavelength. Only two participants presented their CFD simulations. The first was Iowa Institute of Hydraulic Research (IIHR) using the CFD code CFDShip-Iowa (Sadat-Hosseini et al., 2015). The second was University of Zagreb (UZ) using Naval Hydro Pack (Vukcevic and Jasak, 2016). Both participants showed fair prediction of the motions responses, but the discrepancy of added resistance between the CFD simulations and experiments were up to 100 %. Considering the increasing popularity of CFD modelling in ship hydrodynamics and its capacity to model a more complex phenomenon that an ordinary PF approach cannot handle, e.g. water entry and exit, local wave breaking, viscosities etc., there is a strong need of dedicated verification and validation studies for ships in waves with various heading and wave lengths.

The aim of the present study is to conduct verification and validation studies of CFD simulations of motions responses and added resistance in oblique waves. The present study conducts CFD simulations of the KCS in five headings and six wavelengths. The validation is done by comparing the CFD results with experiments from IIHR (Sadat-Hosseini et al., 2015; Sanada et al., 2021) and FORCE Technology (Simonsen et al., 2013). Only 28 out of the 30 test cases are studied. The shortest wave length $\lambda/L_{pp} = 0.5$ at $135\,^\circ$ and $180\,^\circ$ are not studied due to the excessive computational cost. Furthermore, the uncertainties of the experimental data are very large at these two test cases, making conclusion regarding agreement between CFD and experiments difficult. Loss of incident wave amplitude from the inlet to when the wave front reaches the ship due to numerical diffusion is a well know challenge for CFD.

2 METHODOLOGY

The present Unsteady Reynolds Averaged Navier-Stokes (URANS) CFD simulations are performed with the commercial CFD-code STAR-CCM+ v.2020.1 from Siemens (2020). STAR-CCM+ discretizes the governing equations using an unstructured finite-volume method. The code is widely used in the marine industry and is well known for its capabilities within marine applications. The CFD model has previously been validated for calm water resistance calculations in both model and full-scale (Mikkelsen et al., 2019; Mikkelsen and Walther, 2020).

2.1 KCS and Towing Tank Test

The studied ship is the Kriso Container Ship (KCS). The main particulars of the KCS can be seen in Table 1. The KCS is chosen since both experimental data and the hull geometry is publicly available. A definition of the five studied wave headings is illustrated in Figure 1. The present study uses the same ship-fixed coordinate system used by IIHR (Sadat-Hosseini et al., 2015; Sanada et al., 2021) and is seen in Figure 2. The towing tank tests at IIHR have been conducted in the $40 \times 20 \times 3\,\mathrm{m}$ wave basin (Sadat-Hosseini et al., 2015). Unless otherwise mentioned, this same model scale described in Table 1 will be used in all analyses in this paper. The towing tank tests in $0\,^\circ$ heading by FORCE

Table 1: Main particulars.

Name	Symbol	Value
Length between perpendiculars	L_{pp}	2.7 m
Beam	B	0.378 m
Draft	T	0.1268 m
Displacement	Δ	84.00 kg
Speed	U	1.34 m s^{-1}
Vertical center of gravity (from keel)	KG	0.168 m
Longitudinal radius of gyration	k_{xx}	0.39 B
Transverse radius of gyration	k_{yy}	0.25 L_{pp}

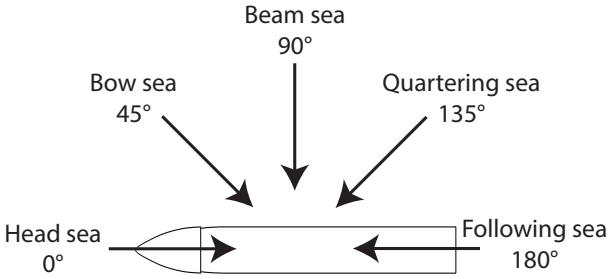

Figure 1: Studied wave headings.

Technology are conducted with a longer $L_{pp} = 4.37\,\text{m}$ model in a $240 \times 12 \times 5.5\,\text{m}$ wave basin.

2.2 Governing Equations

The governing equations of an incompressible Newtonian fluid are the Navier-Stokes equations (Ferziger and Peric, 2002):

$$\frac{\partial u_j}{\partial x_j} = 0 \tag{1}$$

$$\rho\frac{\partial u_i}{\partial t} + \rho u_j \frac{\partial u_i}{\partial x_j} = -\frac{\partial p}{\partial x_i} + \frac{\partial}{\partial x_j}\left(2\mu S_{ij} - \rho\overline{u_j' u_i'}\right) + f_i \tag{2}$$

where u_i is the velocity vector, t is time, p is pressure, μ is dynamic viscosity, $S_{ij} = \frac{1}{2}\left(\frac{\partial u_i}{\partial x_j} + \frac{\partial u_j}{\partial x_i}\right)$ is the mean strain rate, u_i' is the turbulent fluctuating part of the velocity, and f_i is body forces including gravity and wave forcing.

In order to close the problem the Reynolds stresses are modelled using a linear eddy viscosity model. The linear constitutive relationship (Wilcox, 1998) is:

$$-\rho\overline{u_i' u_j'} = 2\mu_t S_{ij} - \frac{2}{3}\rho k \delta_{ij} \tag{3}$$

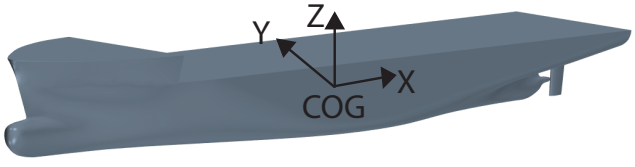

Figure 2: Coordinate system.

where μ_t is the turbulent viscosity, k is the turbulent kinetic energy, and δ_{ij} is Kronecker's delta.

In this study the turbulent viscosity is calculated using the realizable k-ϵ turbulence model (Shih et al., 1995; Siemens, 2020). The k-ϵ model is a two equations model based on the turbulent kinetic energy k and the turbulent dissipation rate ϵ (Wilcox, 1998):

$$\mu_t = \rho C_\mu \frac{k^2}{\epsilon} \tag{4}$$

where C_μ is an empirical constant.

The free surface is resolved using the Volume Of Fluid (VOF) method in STAR-CCM+ (Hirt and Nichols, 1981; Siemens, 2020). Hence, the volume fraction α is assigned and evolves in time with the following transport equation:

$$\frac{\partial \alpha}{\partial t} + \frac{\partial}{\partial x_j}(\alpha u_j) = 0 \tag{5}$$

The transport equation is solved using the High-Resolution Interface Capturing scheme (Muzaferija and Perić, 1997). The effective fluid properties are weighted using the volume fraction:

$$\rho = \alpha \rho_w + (1 - \alpha)\rho_a \tag{6}$$

$$\mu = \alpha \mu_w + (1 - \alpha)\mu_a \tag{7}$$

where ρ_w is the density of the water phase, ρ_a is the density of the air phase and μ_w and μ_a are the corresponding dynamic viscosities. For all simulations, the schemes for the convective and diffusive terms are 2^{nd}-order. The solver for the temporal discretization is a second-order implicit scheme, and the convective Courant number is kept below 0.5 on the free surface. For each time step, eight inner iterations are used to ensure convergence of the non-linear equations.

2.3 Computational Domain and Wave Generation

The shape of the CFD domain is a rectangular box. The top of the domain is set to a pressure outlet in order to allow the air flow to evolve freely. All vertical sides are velocity inlets. When all vertical sides are velocity inlets and not pressure outlets, the heading of the ship can be allowed to change in future manoeuvring simulations. The modelled water depth in the CFD model is 3 m, which is the same as that in the model tests. Since the longest wave length considered in our study is 5.4 m, it is not expected that the water depth has any important effects on the seakeeping and added resistance of the ship. Therefore, the bottom of the domain is treated as a velocity inlet.

The total computational domain contains two parts, namely the forcing zone (or relaxation zone) and the solution zone, see Figure 3 for an illustration. The forcing zone at the outer layer of the computational domain is used to generate the incident regular waves. A smooth-transition function in the form of $\cos^2(x)$ is applied within the forcing zone, so that the flow solution is enforced to be the same as the prescribed incident waves at the outer boundaries (the 4 vertical boundaries), while the forcing becomes zero at the end of the forcing zone, i.e. close to the boundary of the solution zoom. The forcing zone also acts as wave absorbing zone due to the relaxation of the solution towards the targeted incident wave solution at the outer boundaries. In this paper, the Stokes fifth-order waves are used as input waves, which are available from the built-in wave module in STAR-CCM+. The steepness of the incident wave is 1.7 % in order to match the experimental data provided in (Sadat-Hosseini et al., 2015; Sanada et al., 2021). The width of the forcing zone is equal to two times the wavelength of the incident wave. The influence of the forcing zone width has been studies in detail. It is found that a forcing zone width of two incident wavelengths is a good compromise between

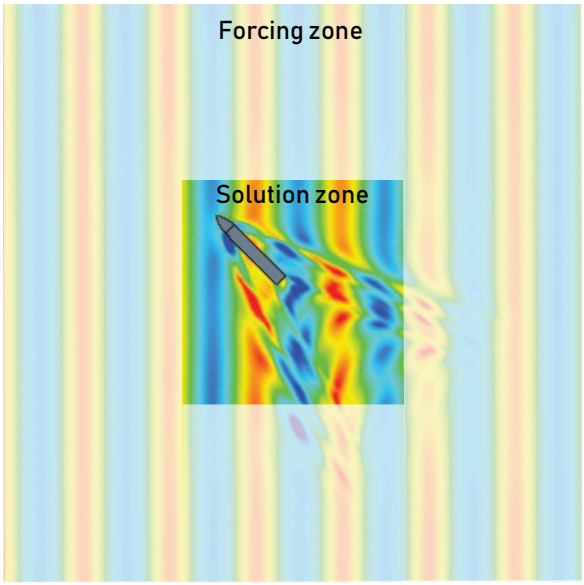

Figure 3: Wave elevation for 45° heading and $\lambda/L_{pp} = 1$.

numerical diffusion, wave reflection and computational cost. A forcing zone width of only one incident wavelength caused significant reflection (not shown). The inner volume, where no forcing is applied, is denoted the solution zone. The size of the solution zone is slightly different for each heading because the combination of generated steady Kelvin wave pattern and unsteady diffraction and radiation waves is different for each heading. However, the size of the solution zone is the same for all wavelength for a given heading. A size of the solution zone of approximately $3L_{pp} \times 3L_{pp}$ is chosen, so it is large enough not to influence the added resistance and seakeeping responses.

2.4 Mesh

The mesh consists of background region and an overset region. The size of the overset domain is determined, so there is always minimum 5 cells from the surface of the ship to the overset boundary. This is recommended by Siemens (2020), in order to ensure that the overset solver accurately can exchange information between the background domain and the overset domain. The size of the overset domain can be seen in Figure 4. The volume mesh consists of hexahedrons in an unstructured grid. The mesh is generated using the trimmer-mesh function in STAR-CCM+ and is aligned with the wave direction. The boundary layer mesh, also called the prism layer mesh, is used on the hull surface in order to ensure accurate estimation of the wall shear stress within the wall function approximation. Three prism layers are used on the ship hull. The quality of the prism layers are inspected to ensure high quality and good transition from the outer prism layer to the core mesh. The wall y^+-values on the hull are mostly in the range of 30–200. The mesh is refined in the important zones including the free surface, near the ship and in the overset overlapping zone. The built-in overset adaptive mesh refinement module in STAR-CCM+ is used to ensure equal cell sizes in the overlapping region between the background and overset mesh. The mesh on the free surface can be seen in Figure 4. The mesh including the ship is moving with constant horizontal speed of 1.34 m/s.

2.5 Motions

In the IIHR experiments (Sadat-Hosseini et al., 2015; Sanada et al., 2021), the ship is fixed in z-rotation (yaw) and y-translation (sway). A sping-mass system is used in the experiments in the x-direction (surge), as described by Sadat-Hosseini et al. (2015). However, the surge motions are small (less than $1\,\%L_{pp}$) and for the Tokyo CFD workshop (Hino et al., 2020), which the experiments are made for, it was recommends to fix the surge in the numerical studies. Therefore, the aim is to make a CFD

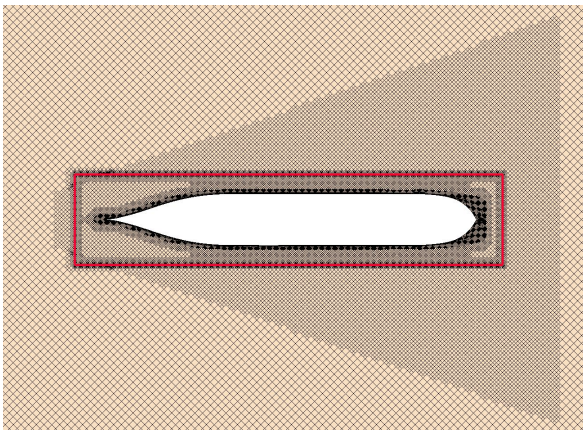

Figure 4: Mesh on the free surface seen from the top for 45° heading and $\lambda/L_{pp} = 1$. The overset boundary is shown in red. Volumetric refinement is seen to resolve the generated Kelvin waves.

model, where only the ship is free in z-translation (heave), y-rotation (pitch) and x-rotation (roll). In the CFD model, the heave, pitch, and roll motions of the vessel are solved using the Dynamic Fluid Body Interaction (DFBI) Multi Body solver in STAR-CCM+ cf. (Ohmori, 1998; Siemens, 2020) and is applied as a rigid translation and rotation of the overset domain mesh. The DFBI Multi Body solver is chosen for its stability and accuracy. Sway is constrained accurately by the motion solver in STAR-CCM+. However, the DFBI solver in STAR-CCM+ version 2020.1 is found to produce an unacceptable drift in the constrained yaw. Besides the drift, constraining the yaw motion by the built-in motion module in STAR-CCM+ makes the roll response non-physical. Therefore, the yaw and surge motions are constrained using implementations by the authors. The surge motion is constrained by applying a concentrated x-force at each time step in the center of mass equal to the integrated shear and pressure forces acting on the hull with opposite sign. With this implementation, the speed of the ship never deviates more than 0.1 % from the target ship speed. Since the integrated x-force is calculated each time step, the implementation allows the ship speed to be non-constant in future studies of, for instance, manoeuvring simulations in waves and self-propulsion simulations in waves. The yaw motion is constrained by applying a concentrated z-moment and a torsional spring around the z-axis of the ship. The magnitude of the applied concentrated z-moment is equal to the integrated z-moment of the ship with opposite sign. The torsional spring constant is set to 20 kNm/deg in order to ensure a small yaw angle and a natural yaw frequency far from the natural frequencies of the motions and incident waves. The magnitude of the concentrated z-moment is approximately 50 times larger than the z-moment from the torsional spring. With this implementation, the simulated yaw angle never exceeds 0.01 deg and it is found not to influence the other motions.

2.6 Post-Processing of the Results

The main output from the simulations are time histories of heave (Z), pitch (θ), roll (ϕ), and total resistance (R). The resistance is the integrated shear stress and pressure on the hull in the x-direction. An example of a resistance time history is shown in Figure 5. From an instant, where the solution ($s(t)$) has periodically steady outputs, an integer number of encounter periods (T_e) are fitted to a 4-term Fourier series:

$$s(t) = a_0 + a_1 \cos(\omega_1 t) + b_1 \sin(\omega_1 t) + ... + a_4 \cos(\omega_4 t) + b_4 \sin(\omega_4 t) \tag{8}$$

where $\omega_k = 2\pi f_e k$, and f_e is the encounter frequency. Each fit is visually inspected to ensure that the fit is representable of the time history and that the fitting window does not start before the time history has stabilized. For the time history shown in Figure 5, the fit only uses the time history for $t/T_e = 9 - 15$. Based on the Fourier coefficients from these fits, the amplitudes (A_k) for heave, pitch,

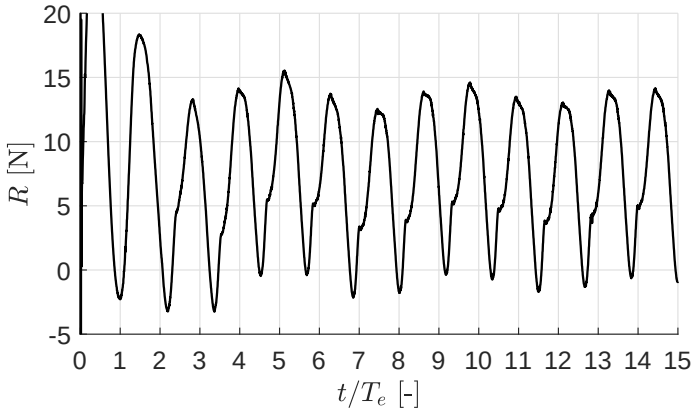

Figure 5: Time history of the measured resistance (R) as function of time non-dimensionalized with encounter period (T_e) at 45° heading and $\lambda/L_{pp} = 1$.

roll, and resistance are calculated using:

$$A_k = \sqrt{a_k^2 + b_k^2} \tag{9}$$

where k is the Fourier term.

The same procedure is used in the Tokyo workshop (Hino et al., 2020) allowing for direct comparison. The present study only focuses on the added resistance and the first amplitude of heave (Z_1), pitch (θ_1), roll (ϕ_1). The added resistance (σ_{aw}) is defined as

$$\sigma_{aw} = \frac{R_0 - R_{CW}}{\frac{\rho A^2 B^2}{L_{pp}}} \tag{10}$$

where R_0 is the zero-th amplitude (mean) resistance using Equation (8) and R_{CW} is the calm water resistance.

For the validation, the amplitudes are non-dimensionalized with the incident wave amplitude that actual reaches the ship and not the target wave amplitude, which is specified at the domain boundaries. The added resistance will also be calculated using the actual wave amplitude.

2.7 Grid Convergence Index

For the verification study of the CFD model, the discretization error is estimated using the Grid Convergence Index (GCI) method (Celik et al., 2008) which is based on Richardson extrapolation, cf. (Richardson, 1910; Richardson and Gaunt, 1927). The apparent order (p) is calculated by:

$$p = \frac{1}{\ln(r_{21})} \left| \ln \left| \frac{\epsilon_{32}}{\epsilon_{21}} \right| + q(p) \right| \tag{11}$$

$$q(p) = \left(\frac{r_{21}^p - s}{r_{32}^p - s} \right) \tag{12}$$

$$s = \operatorname{sgn}\left(\epsilon_{32}/\epsilon_{21}\right) \tag{13}$$

where r are refinement ratios, $\epsilon_{32} = \phi_3 - \phi_2$, $\epsilon_{21} = \phi_2 - \phi_1$, s is a sign indicator, and ϕ_k denotes the solution on the k-th mesh. $q(p) = 0$ for $r = \text{const}$. The extrapolated asymptotic value is calculated as:

$$\phi_{ext}^{21} = \frac{r_{21}^p \phi_1 - \phi_2}{r_{21}^p - 1} \tag{14}$$

Table 2: Frequencies of the natural motions of the ship predicted by the present CFD model.

Roll, without forward speed	f_ϕ	0.27 Hz
Roll, frequency with forward speed	$f_{\phi,U}$	0.33 Hz
Heave/pitch, without forward speed	$f_{Z\theta}$	1.11 Hz
Heave/pitch,with forward speed	$f_{Z\theta,U}$	1.05 Hz

Different error estimates can now be calculated. The approximate relative error is:

$$e_a^{21} = \left| \frac{\phi_1 - \phi_2}{\phi_1} \right| \tag{15}$$

$$e_a^{31} = \left| \frac{\phi_1 - \phi_3}{\phi_1} \right| \tag{16}$$

The extrapolated relative error is:

$$e_{ext}^{21} = \left| \frac{\phi_{ext}^{12} - \phi_1}{\phi_{ext}^{12}} \right| \tag{17}$$

The GCI for the fine and medium mesh is calculated as follows using the safety factor of 1.25 recommended by Roache (1998):

$$GCI_{Fine}^{21} = \frac{1.25 e_a^{21}}{r_{21}^p - 1} \tag{18}$$

Equation (18) is extended to the GCI for the medium and coarse mesh:

$$GCI_{Medium}^{21} = \frac{1.25 e_a^{21} r_{21}^p}{r_{21}^p - 1} \tag{19}$$

$$GCI_{Coarse}^{31} = \frac{1.25 e_a^{31} r_{31}^p}{r_{31}^p - 1} \tag{20}$$

The GCI values are used as an estimate of discretization errors, since they are a measure of the relative discrepancy between the computed value and the asymptotic numerical value. Please note that this method does not identify the exact discretization error, but just an estimate(Roache, 1998).

3 RESULTS

This section consists of five subsections. Firstly, motion decay studies of heave, pitch, and roll. Secondly, a verification study of the estimated spatial and temporal discretization errors of the CFD model estimating the motions responses and added resistance in oblique waves. Thirdly, a verification of the wave generation in the empty CFD tank is conducted to study the loss of incident wave amplitude when progressing the waves in an empty CFD wave tank. Fourthly, the results of the verified CFD model are validated by comparison with experimental results and other available numerical results from the literature. Lastly, the present CFD results as function of the wave heading and wavelength are discussed.

3.1 Motion Decay Studies

Heave, pitch, and roll decays are conducted in CFD using the input specified in Table 1. Decay tests are performed both with and without forward speed. The results of the decay tests are shown in Table 2 and the results without forward speed are similar to the results by Sanada et al. (2021). Sanada et al. (2021) does not present natural motion frequencies with forward speed. However, the natural roll period in Sadat-Hosseini et al. (2015) is 0.23 Hz, which is approximately 15 % lower than what is

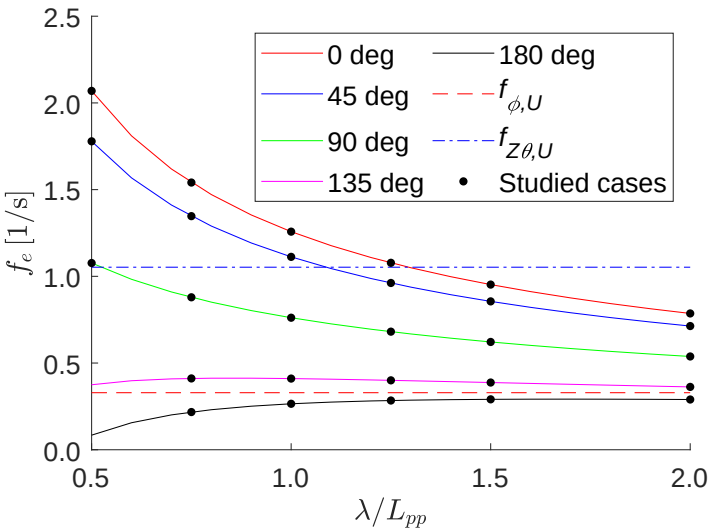

Figure 6: Encounter frequency (f_e) as function of non-dimensional wave length for different headings.

found in the present CFD calculations and in the experiments by Sanada et al. (2021). The reported gyrospopic radius k_{xx} is the same in all studies. The reason for this discrepancy is unknown. It is found that the natural roll frequency increases approximately 22 %, when forward speed is included. Furthermore, the natural heave and pitch frequency is decreasing with approximately 5 % with a forward speed of 1.24 m/s. The 22 % increase of the roll period is significant. Similar results are found by Irkal et al. (2019). Ikeda et al. (1978) discusses the influence of the different roll damping coefficients at forward speed. The natural frequencies together with encounter frequencies of the studies cases can be seen in Figure 6.

3.2 Verification of Mesh and Time Step

The verification studies are conducted for a wavelength of $\lambda/L_{pp} = 1.00$ at 45 ° heading. This is considered one of the most challenging test cases for the CFD solver. This test case has very large motions and added resistance partly due to fact that the encounter period is close the natural pitch and heave period as seen in Figure 6. For both the mesh and time step convergence studies, the mean of the resistance signal and first-order amplitude of the dimensional heave, pitch, and roll signal are analysed. The results will not be non-dimensionalized. This causes the estimated spatial and temporal discretization errors to include both the sensitivity of the resolution on the effect of loss of incident wave amplitude and on the motion responses and local flow around the ship.

3.2.1 Mesh Convergence Study

Three meshes are tested to estimate the spatial discretization error using the GCI procedure described in Section 2.7. The refinement ratios are determined using the cubic root of the total cell count for each mesh. The three meshes are generated by changing the base size, which affects the size of all cells besides the prism layer cells. A constant aspect ratio of eight is chosen between horizontal and vertical grid spacing in the free surface refinement zone. For all mesh convergence simulations, a time step equal to 750 time steps per incident wave period is used. With this time step size, the Courant number on the free surface for all meshes is well below the value of 0.5 as suggested by Siemens (2020). The obtained GCI's are shown in Table 3. Mesh 2 has 68 cells per wavelength and 9 cells per wave height in the free surface refinement zone. This is slightly fewer cells than what is recommended by Siemens (2020). However, Mesh 1 has 90 cells per wavelength and 12 cells per wave height and the influence on the results is less than 2 %, as seen in Table 3. Mesh 1 has approximately double as many cells as Mesh

Table 3: Grid convergence index values for the estimated spatial discretization error for heave (Z_1), pitch (θ_1), and roll (ϕ_1), respectively. The simulation time is based on 80 cores using Intel Xeon Gold 6242R CPUs.

	Number of cells	Simulation time	Z_1	θ_1	ϕ_1
Mesh 1	12.7×10^6	70 hours	0.7 %	0.1 %	2.7 %
Mesh 2	6.7×10^6	40 hours	1.7 %	0.2 %	4.4 %
Mesh 3	1.5×10^6	6 hours	13.8 %	15.6 %	14.0 %

2. Furthermore, the estimated spatial discretization errors of Mesh 2 are smaller than the average standard deviation of the experiments by Sanada et al. (2021). Because of this, it is decided to use Mesh 2 settings for all further simulations, since it is considered the best compromise between spatial discretization errors and computational cost. Please note that the mesh settings will result in a larger number of cells for the shorter waves and fewer cells for the longer waves. This is because the size of the solution zone is the same for all waves for a given wavelength, where the width of the forcing zone is equal to two incident wavelengths. The difference in resistance between Mesh 1 and Mesh 3 is less than 0.3 % even though there is more than 8 times more cells in Mesh 1. The resistance using Mesh 2 is 2.3 % higher than when using Mesh 1. This indicates a low sensitivity to the mesh. However, the GCI method considers this oscillatory convergence behaviour. With oscillatory convergence behaviour, the resulting GCIs for resistance become very large, even though the differences in resistance between the three meshes are small. However, this very large GCIs are not considered representative for the spatial discretization error for the resistance. This is an indication that the GCI approach has its limitations. As discussed in Section 2.7 and by Roache (1998), the GCI approach only gives estimations of the discretization errors an not the exact discretization errors.

3.2.2 Time Step Convergence Study

In order to quantify the temporal discretization error, simulations are conducted with varying time step sizes using the settings from Mesh 2 from the previous subsection. It is decided to non-dimensionalize the time step with the incident wave period and not the encounter period, since the incident wave period is independent of wave heading. Three time step sizes are tested to estimate the temporal discretization errors using the GCI procedure described in Section 2.7. The results in Table 4 show in generel quite low estimated temporal discretization errors. Based on the results, it is decided to use a time step corresponding to 750 time steps per incident wave period for all cases, since the estimated temporal discretization errors are less than 1.2 % for all motion responses and added resistance in the convergence study. This time step is considered the best compromise between computational cost and temporal discretization error. To use 750 time steps per incident wave period will cause a higher number of time steps per encounter period for the $90\,^\circ, 135\,^\circ$, and $180\,^\circ$ headings, since the encounter periods are $30 - 400\,\%$ larger for these headings. Therefore, 750 time step per incident wave period is considered a conservative choice of time step size. The encounter periods for the $0\,^\circ$ heading are only $9 - 14\,\%$ smaller than for the $45\,^\circ$ heading. This is considered small enough not to influence the sensitivity of the time step. Furthermore, the verification study is conducted for a test case, where the encounter frequency is close to the natural heave and pitch frequency causing complex flow phenomena and strong variation in time. The sensitivity of the time step is considered higher at this resonance test case than a non-resonance test case. The sum of the spatial and temporal discretization errors is less than 5 %, which is less than the average standard deviation of the experiments by Sanada et al. (2021).

Table 4: Grid convergence index values for the estimated temporal discretization error for heave (Z_1), pitch (θ_1), roll (ϕ_1), and resistance (R). The simulation time is based on 80 cores using Intel Xeon Gold 6242R CPUs.

Time steps per wave period	Simulation time	Z_1	θ_1	ϕ_1	R
1200	64 hours	0.2 %	0.0 %	0.2 %	0.3 %
750	40 hours	1.1 %	0.0 %	0.5 %	0.7 %
500	27 hours	5.7 %	2.4 %	0.5 %	1.3 %

3.3 Verification of empty wave tank

Numerical diffusion causing loss of incident wave amplitude is a common challenge in CFD when modeling wave propagation over a large distance. In order to quantify the amplitude of the incident wave, when it encounters the ship, simulations of the wave tank without the ship are conducted. The simulations are conducted using the mesh and time step settings found in the previous verification section. The empty wave tank domains have the same sizes and is moving with the ship speed identical to the calculations with the ship. The wave amplitude is measured at the position, where the ships center of gravity would be. The amplitude is determined using the Fourier fitting procedure described in Section 2.6. The loss of incident wave amplitude in percent can be seen in Table 5. An example of the obtained and target wave profile can be seen in Figure 7. The results show that the wave generation works quite well with the selected settings, including the size of wave forcing zone, forcing strength, computational domain size, and other settings. Besides the shortest waves, most of the test cases have a loss of wave amplitude lower than 4 %. For the shortest wave, the loss of incident wave amplitude is up to 12 %. This illustrates why it is important to non-dimensionalize the motion responses and added resistance with the obtained incident wave amplitude and not the incident wave amplitude specified on the domain boundary. There is a clear tendency that the shorter the wave length, the larger the loss of amplitude. This is because the size of the solution zone is independent of the wavelength. Therefore, the shorter the wave, the larger number of incident waves are present in the solution zone. Due to the presence of numerical diffusion, the larger distance relative between inlet and ship, the more energy is dissipated, leading to larger loss of wave amplitude. This loss could be reduced by choosing a smaller time step and a finer mesh. However, this will increase the computational cost significantly. Another solution could be to use a smaller solution zone. In addition to resolving the unsteady waves, the computational zone has to be sufficiently large to resolve the steady waves generated by the ship and minimize the reflection of the steady waves by the computational boundaries. Since the target steepness of the incident waves are very small and that the added resistance is mainly a second-order effect in wave steepness cf. Faltinsen (1993), it is expected that the loss of incident-wave amplitude has little influences on non-dimensional added resistance (Equation (10)). Therefore, the amplitudes in Table 5 are considered acceptable.

Table 5: Loss of incident wave amplitudes in percent at the ships center of gravity position for different headings and wavelengths.

		λ/L_{pp}					
		0.50	0.75	1	1.25	1.50	2.00
Heading	0 °	12.0 %	7.2 %	3.2 %	2.1 %	1.9 %	1.3 %
	45 °	11.7 %	6.5 %	2.8 %	1.7 %	1.6 %	1.1 %
	90 °	10.2 %	3.4 %	2.1 %	0.7 %	1.0 %	0.9 %
	135 °		5.9 %	2.7 %	1.4 %	1.4 %	1.2 %
	180 °		6.1 %	2.6 %	1.4 %	1.5 %	1.1 %

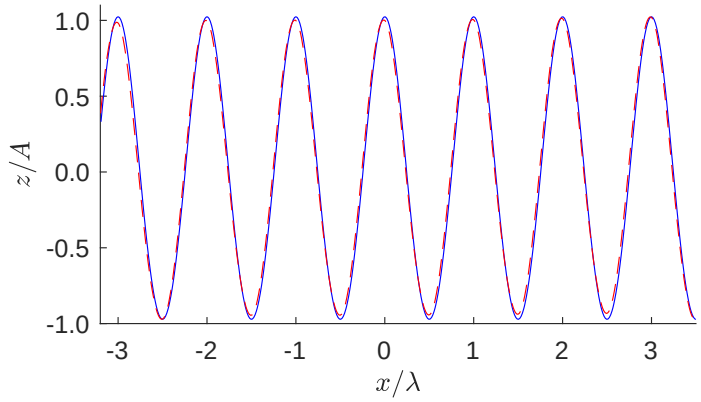

Figure 7: Comparison of theoretical (solid blue curve) and actual (red dashed curve) wave profile though the center plan for the $\lambda/L_{pp} = 1$ wave at 45° heading.

3.4 Validation

3.4.1 0 ° Heading

The present CFD model is validated for each of the five studied headings in the following five sections. The present CFD results are compared with up to three sets of Experimental Fluid Dynamics (EFD) data. For all headings, two set of experimental data are from IIHR by Sadat-Hosseini et al. (2015) and Sanada et al. (2021). The study by Sanada et al. (2021) also presents a calculated standard deviations for the $\lambda/L_{PP} = 1.0$ waves. These standard deviations are included as error bars in Figures 8 to 12. For the 0 ° heading, results from FORCE Technology by Simonsen et al. (2013) are also included in the comparison as (FORCE). Furthermore, the present CFD results are compared with potential flow (PF) results by Sadat-Hosseini et al. (2015) who used the 3D PF code FATIMA (Bunnik, 1999). At the Tokyo CFD workshop in 2015, only two participants submitted their CFD results for the case with motion responses and added resistance in oblique waves. The first participant is IIHR using the CFD code CFDShip-Iowa Sadat-Hosseini et al. (2015). The second participant is University of Zagreb (UZ) using Naval Hydro Pack (Vukcevic and Jasak, 2016). However, at the workshop only the $\lambda/L_{PP} = 1.0$ waves were studied and included in the present comparison. Translatory and rotational motion responses are non-dimensionalized by the actual wave amplitude (A) from Section 3.3 and wave steepness (kA) respectively, where $k = \frac{2\pi}{\lambda}$. The added resistance is calculated using Equation (10).

The comparison of the present CFD results, previously reported CFD and PF results, and three sets of experimental data for the 0 ° heading can be seen in Figure 8. For this heading, the agreement between the three experimental data sets is good. Both the present CFD, UZ CFD and PF motions responses agree very well with the experiments. In general, the present CFD results show slightly better agreement in motion responses than the PF results, especially for the longer waves. As shown in Figure 6, the encounter frequency of the $\lambda/L_{pp} = 1.25$ wave is very close to the natural heave and pitch frequencies causing resonance. The CFD by IIHR and the PF results overestimates the added resistance near the resonance area with approximately 45 %. However, the added resistance estimated by the present CFD model is within the standard deviation of the experiments by Sanada et al. (2021).

3.4.2 45 ° Heading

Figure 9 shows the comparison of the present CFD results, previously reported CFD and PF results, and two sets of experimental data for the 45 ° heading. The heave responses shown in Figure 9a, predicted by both the present CFD and PF agree very well with the experiments. The largest deviation is observed for the longest wave. However, the deviation is still smaller than the difference between the two sets of experiments. For the pitch response, shown in Figure 9b, both the present CFD and PF

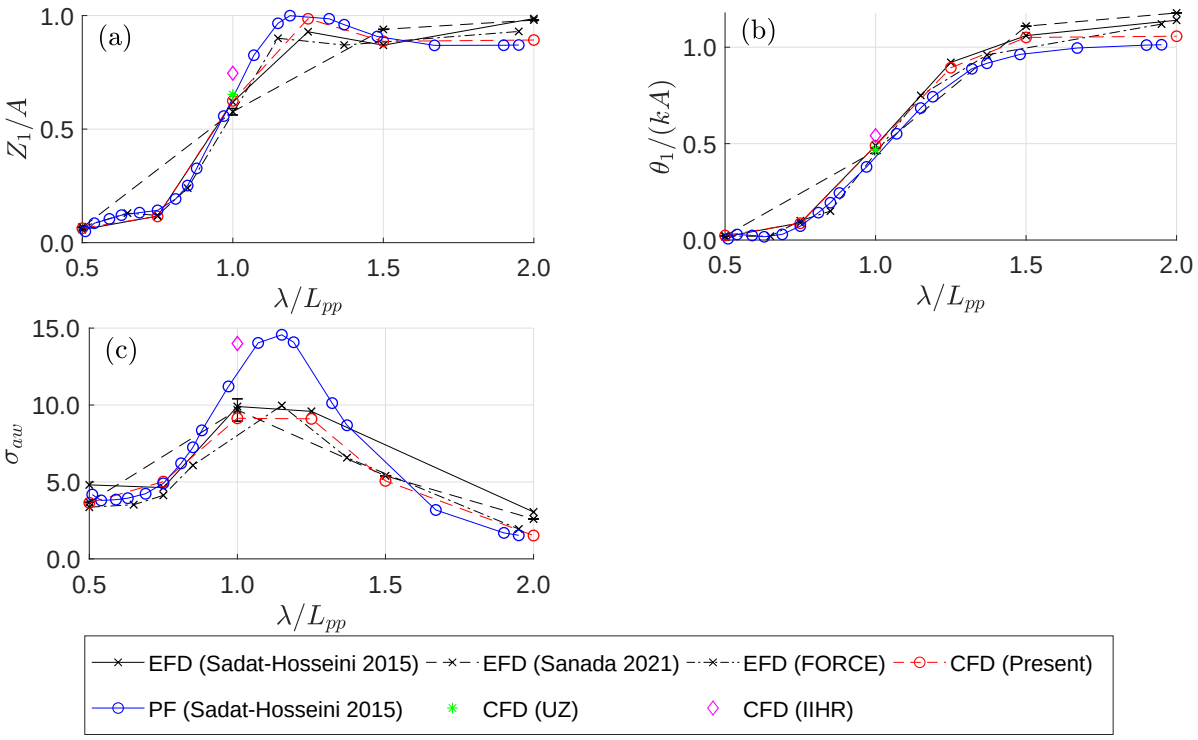

Figure 8: Comparison of results for 0 ° heading as function of non-dimensional wavelength (λ/L_{pp}). (a) Heave, 1st amplitude (Z_1); (b) Pitch, 1st amplitude (θ_1); (c) Added resistance (σ_{aw}).

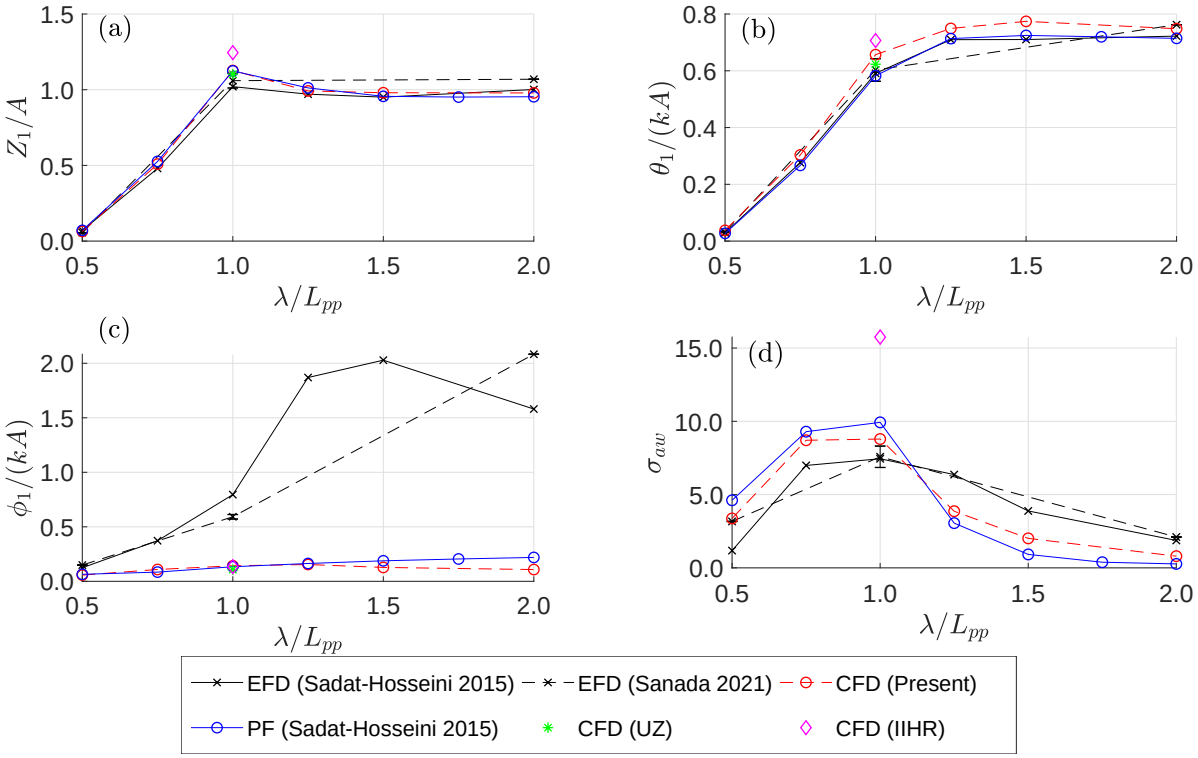

Figure 9: Comparison of results for 45 ° heading as function of non-dimensional wavelength (λ/L_{pp}). (a) Heave, 1st amplitude (Z_1); (b) Pitch, 1st amplitude (θ_1); (c) Roll, 1st amplitude (ϕ_1); (d) Added resistance (σ_{aw}).

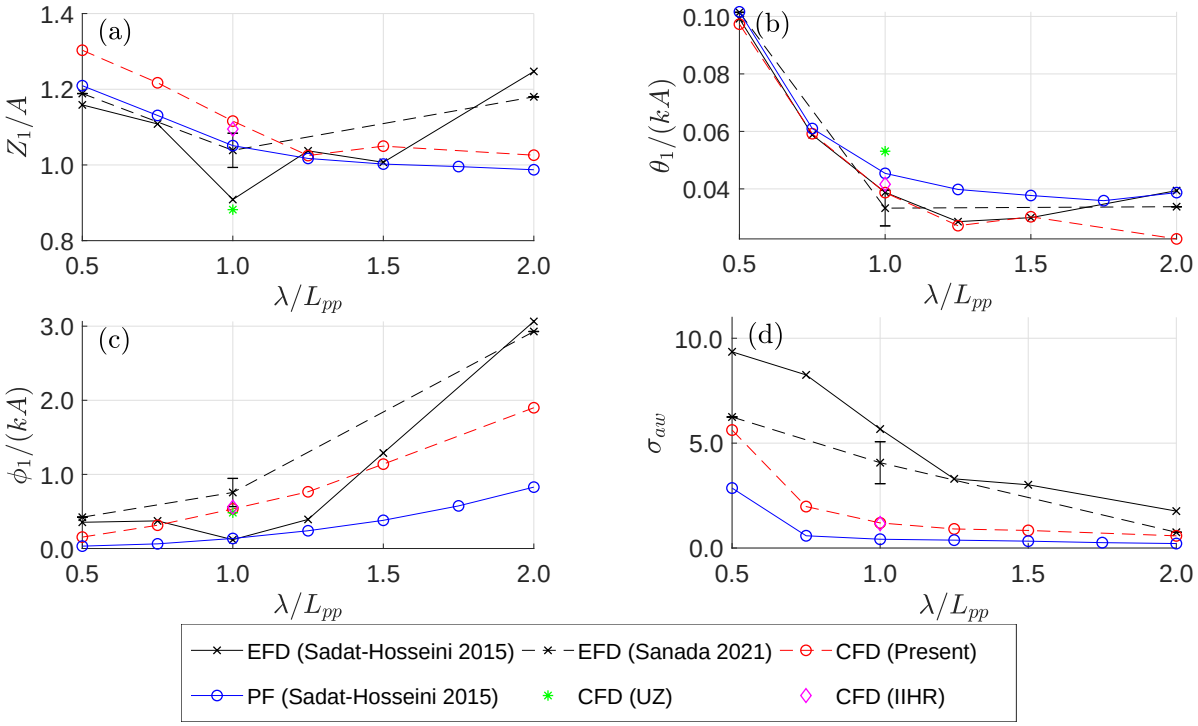

Figure 10: Comparison of results for 90 ° heading as function of non-dimensional wavelength. (a) Heave, 1st amplitude (Z_1); (b) Pitch, 1st amplitude (θ_1); (c) Roll, 1st amplitude (ϕ_1); (d) Added resistance (σ_{aw}).

agree well with the experiments for the two shortest waves. For the longer waves, both the PF and the present CFD results approaches an asymptotic limit. The PF agrees excellently with the pitch found in the EFD by Sadat-Hosseini et al. (2015) for all wavelengths and approaches an asymptotic value very similar to the value found by the experiments by Sadat-Hosseini et al. (2015) at $\lambda/L_{pp} = 2.0$. The present CFD approaches a value similar to the value found in the experiments by Sanada et al. (2021) at $\lambda/L_{pp} = 2.0$. The CFD by UZ predicts the heave and pitch responses well, where the CFD by IIHR overestimates the heave and pitch responses with approximately 10 %. The roll responses found in the experiments are much larger than any of the numerical methods as seen in Figure 9c. The roll responses predicted by the PF and all three CFD approaches agrees well with each other, but not with the experiments. Even the smallest encounter frequency of the studied waves in 45 ° heading is 0.72 Hz. This is more than double the natural roll period (0.33 Hz) with forward speed. It is not clear why the experimental roll responses are about one order of magnitude higher than numerical results. This needs more dedicated experimental studied in the future and is out of the scope of the present study. When the wavelength is increased, the encounter frequency is decreasing for the 45 ° heading as seen in Figure 6. Therefore, it is expected that the roll responses should only increase slowly while the wavelength is getting larger and the encounter frequency becomes closer to the natural roll frequency. This is the behaviour of all the numerical results in Figure 9c. In general, both the PF and the present CFD overestimates the added resistance at the shorter waves and underestimates the added resistance at the longer waves as seen in Figure 9d. However, the added resistance from the present CFD is closer to the experiments for all wavelengths than the PF results. For the $\lambda/L_{pp} = 1.0$ wave, the CFD by IIHR overestimates the added resistance with approximately 100 %, where the present CFD overestimates the added resistance with approximately 18 %. The standard deviation of the experimental added resistance by Sanada et al. (2021) is 10.7 % at this wave.

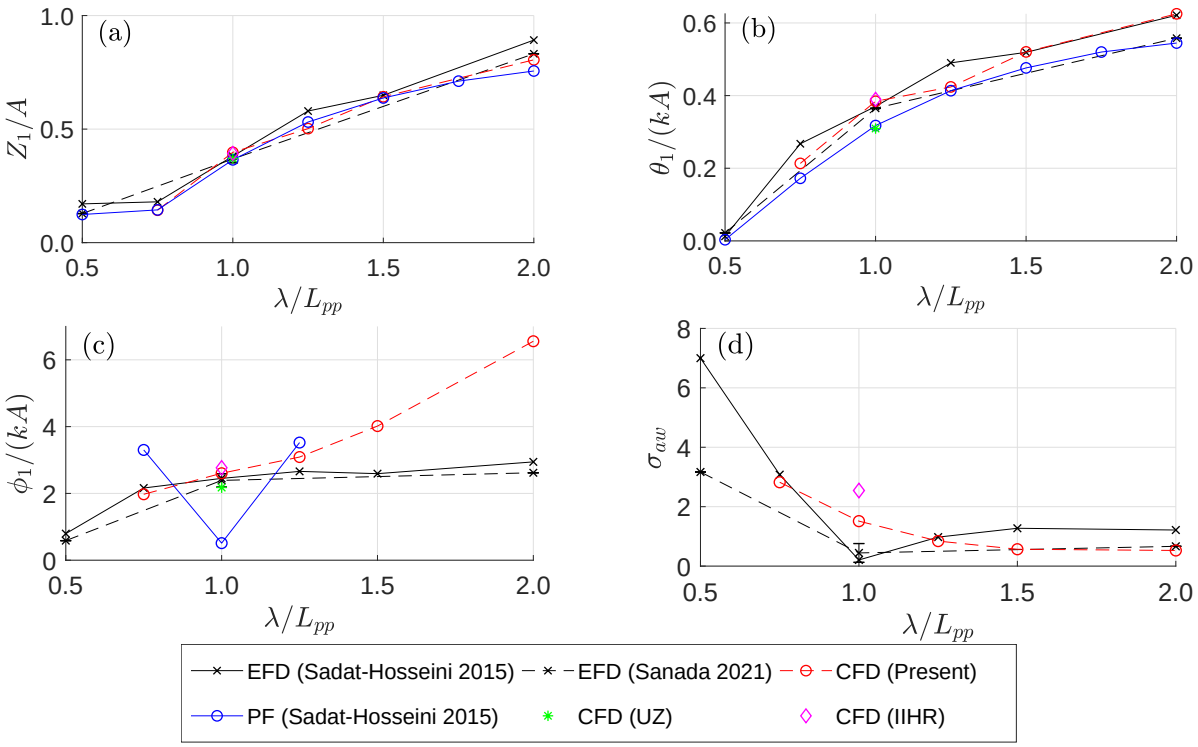

Figure 11: Comparison of results for 135 ° heading as function of non-dimensional wavelength; (a) Heave, 1st amplitude (Z_1); (b) Pitch, 1st amplitude (θ_1); (c) Roll, 1st amplitude (ϕ_1); (d) Added resistance (σ_{aw}).

3.4.3 90 ° Heading

For the 90 ° heading, the comparison of the present CFD results, previously reported CFD and PF results, and two sets of experimental data can be seen in Figure 10. The encounter frequency of the $\lambda/L_{pp} = 0.5$ wave is close to the natural heave and pitch frequency as see in Figure 6. Therefore, it would be expected to have maximum added resistance, heave and pitch responses at this this wave. Both the present CFD and PF show this trend. However, the experiments only show maximum pitch and added resistance at $\lambda/L_{pp} = 0.5$ as seen in Figure 10. For heave, shown in Figure 10a, the two experimental results show a maximum heave response at $\lambda/L_{pp} = 2.0$. Both the PF and the present CFD show a heave response approaching an asymptotic value close to unity. This is the expected behaviour for long waves that have passed the heave/pitch resonance point. For the heave response, the PF results have a slightly better agreement with the experiments than the present CFD does. However, the present CFD agrees better with the experiments than PF for pitch. The disagreement between the experiments for roll, shown in Figure 10c, is larger than for the heave and pitch. In general, PF underestimate the roll response. This is unexpected since the PF based on the work by Bunnik (1999), which does not include viscous effect and therefore viscous roll damping. It is unknown to the authors, if additional roll damping has been added to the PF calculation presented by Sadat-Hosseini et al. (2015). The roll responses predicted by the present CFD are between the experimental results by Sanada et al. (2021) and Sadat-Hosseini et al. (2015) for the $\lambda/L_{pp} = 1.0$. The CFD by UZ slightly underestimate the heave and overestimate the pitch relative the experimental results. The predicted roll response of the UZ CFD is very similar to the present CFD results and the CFD results by IIHR. Both PF and the present CFD underestimates the added resistance as seen in Figure 10d. However, the underestimation by the present CFD is smaller than the underestimation by PF.

3.4.4 135 ° Heading

The comparison of the present CFD results, previously reported CFD and PF results, and two sets of experimental data for the 135 ° heading can be seen in Figure 11. The agreement between the two sets of experiments is fair for the three motion responses. However, for the added resistance, the disagreement is large. In general, the predicted motion responses of the three CFD approaches are similar. The heave and pitch responses are very well predicted by both the CFD and PF as shown in Figure 11a and Figure 11b. The roll responses of the shortest waves are predicted very well by the present CFD as seen in Figure 11c. However, for the longer waves, the present CFD overpredicts the roll response. As seen in Figure 6 the encounter frequencies for longer waves at 135 ° heading are getting close to the natural roll frequency of the ship. Therefore, the roll response is expected to increase, when the wavelength is increased. A possible reason for the disagreement in roll response between the present CFD and EFD at the long waves, is the underestimation of roll damping by the present CFD. It could also be due to a discrepancy in k_{xx} and therefore the natural roll frequency. Since the encounter frequency of the $\lambda/L_{pp} = 2.0$ wave is close to the natural roll frequency, a small difference in the natural roll frequency can have a significant influence on the roll response. The disagreement between PF and experiments for roll responses is significant and the trend of the roll response predicted by PF is difficult to explain. In addition, for roll responses, the PF results are only available for three wave lengths, cf. (Sadat-Hosseini et al., 2015). The agreement between the present CFD and EFD for added resistance, shown in Figure 11d, is good considering the uncertainties of the experiments. Both sets of experimental results show a minimum added resistance at $\lambda/L_{pp} = 1.0$. The trend of the present CFD prediction is a more smooth curve approaching an asymptotic value very similar to the EFD value found by Sanada et al. (2021). The overestimation of the CFD by IIHR is larger than the overestimation by the present CFD at $\lambda/L_{pp} = 1.0$. PF results for added resistance in 135 ° heading are not availiable by Sadat-Hosseini et al. (2015).

3.4.5 180 ° Heading

In general, the encounter frequencies for the waves in the 180 ° heading are small. Especially the $\lambda/L_{pp} = 0.5$ wave has a very low encounter frequency, which makes it challenging for the EFD to obtain long enough time series to extract reliable results for added resistance enough due to limited length of the tank. Figure 12 shows the comparison of the motion responses and added resistance predicted by the present CFD model, previously reported CFD and PF, and two sets of experimental data for the 180 ° heading. The agreement between the two sets of experimental results is good for the motion responses besides the shortest $\lambda/L_{pp} = 0.5$. Therefore, the present CFD simulations have not been conducted for the $\lambda/L_{pp} = 0.5$ wave. The added resistance found by the two experiments are quite different as seen in Figure 12c. The experiments by Sadat-Hosseini et al. (2015) shows a trend of increasing added resistance, when the wavelength is increased, while the EFD by Sanada et al. (2021) shows the opposite trend of decreasing added resistance. Therefore, it is difficult to comment on the agreement of added resistance between CFD and EFD at the 180 ° heading. However, it can be concluded that the discrepancy between CFD and EFD is similar or smaller than the discrepancy between the two sets of experiments. More experiments with lower uncertainty are required in order to be able to validate results of numerical tools for the 180 ° heading. In general, the predicted motion responses of the three CFD approaches are similar. The predicted heave and pitch responses by PF and CFD are in good agreement with the experiments as seen in Figure 12a and Figure 12b. However, the pitch response for the $\lambda/L_{pp} = 2.0$ wave is overpredicted by the present CFD.

3.4.6 Influence of Wave Heading

The predicted motion responses and added resistance by the present CFD model as function of wave heading and wavelength are shown in Figure 13. The heave results seen in Figure 13a show a general trend of approaching an asymptotic value close to unity for the long waves. This is expected because

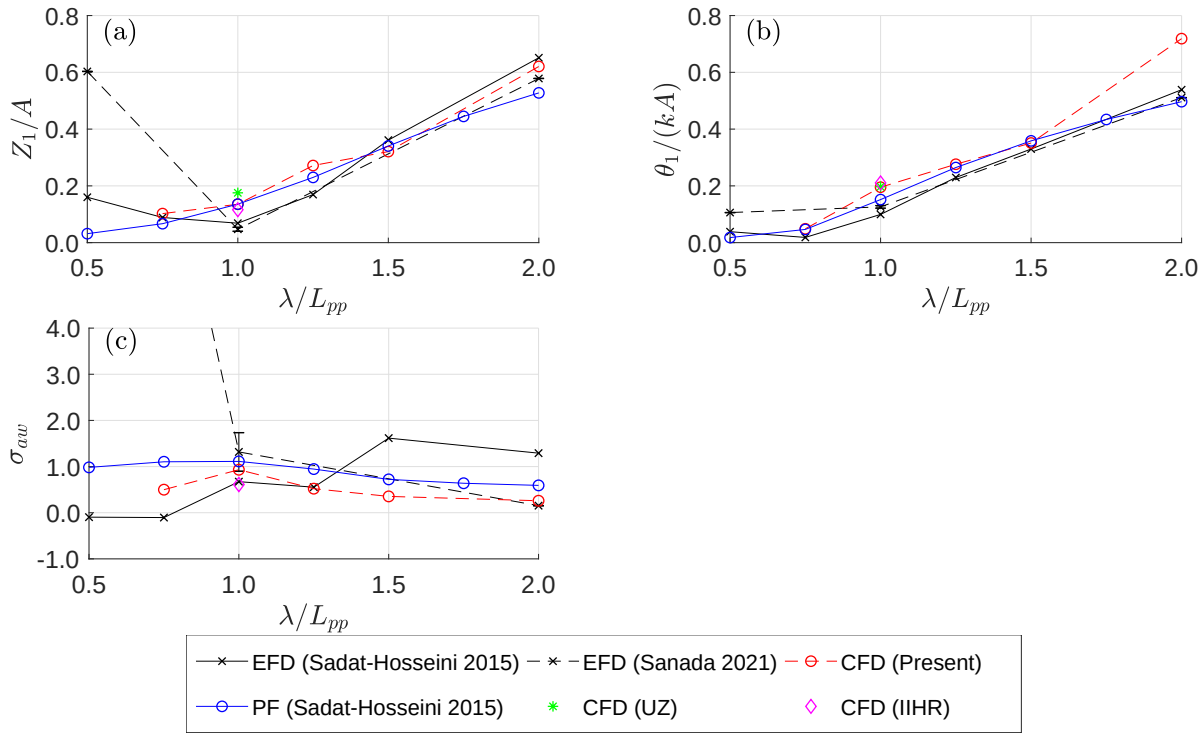

Figure 12: Comparison of results for 180 ° heading as function of non-dimensional wavelength. (a) Heave, 1st amplitude (Z_1); (b) Pitch, 1st amplitude (θ_1); (c) Added resistance (σ_{aw}).

when the waves are much longer than the ship, the ship will simply follow the wave elevation. When the waves are very short, the heave response will approach zero, since the waves are too short to excite the motions of the ship. The heave responses for the 90 ° heading have a maximum heave response at $\lambda/L_{pp} = 0.5$, since the encounter frequency is very close to the natural heave frequency as seen in Figure 6. If shorter waves were to be tested in the 90 ° heading, it would be expected that the heave response would decrease and approach zero similarly to the behaviour in other headings. The encounter frequency of the $\lambda/L_{pp} = 1.25$ wave at the 0 ° heading and the $\lambda/L_{pp} = 1.0$ wave at the 45 ° heading are also close to the natural heave frequency. This is why the heave responses are maximum at those waves as seen in Figure 13a. The heave responses in the 135 ° heading and especially the 180 ° heading are smaller in magnitude than the other headings since the encounter frequencies are further away from the natural heave frequency as seen in Figure 6.

The results for the pitch responses on Figure 13b show minimum pitch response at the shortest $\lambda/L_{pp} = 0.5$ wave for all headings besides the 90 ° heading. As in the case for heave, this is caused by the similarity of the encounter frequency of the $\lambda/L_{pp} = 0.5$ at the 90 ° heading and the natural pitch frequency, which is approximately the same as the natural heave frequency. For shorter waves than $\lambda/L_{pp} = 0.5$, the pitch response is expected to approach zero similarly to the other headings, since the waves become too short to cause a pitching moment to ship. However, the magnitude of the pitch responses in 90 ° are very small, since the ship is sailing in beam sea, where the wave length is very long relative to the beam of the ship. The observed pitch is caused by the fact that the ship is not bow-stern symmetric and because the forward speed effect leads to asymmetric pressure distribution at bow and stern. For long waves, the pitch responses for the 0 ° heading approach an asymptotic value close to one. The pitch responses for the 180 ° are expected to do the same for longer waves than the ones presently studied. For long waves, the pitch responses for the 45 ° and 135 ° heading approach an asymptotic value close to $1/\sqrt{2}$.

The roll responses in Figure 13c show extremely small roll responses at the 0 ° and 180 ° heading. This makes good sense since the flow is almost symmetric along the center plane at these headings. The roll responses for the 45 ° heading are very small, because the encounter frequencies in this heading are much smaller than the natural roll frequency as seen in Figure 6. The roll responses for the 90 °

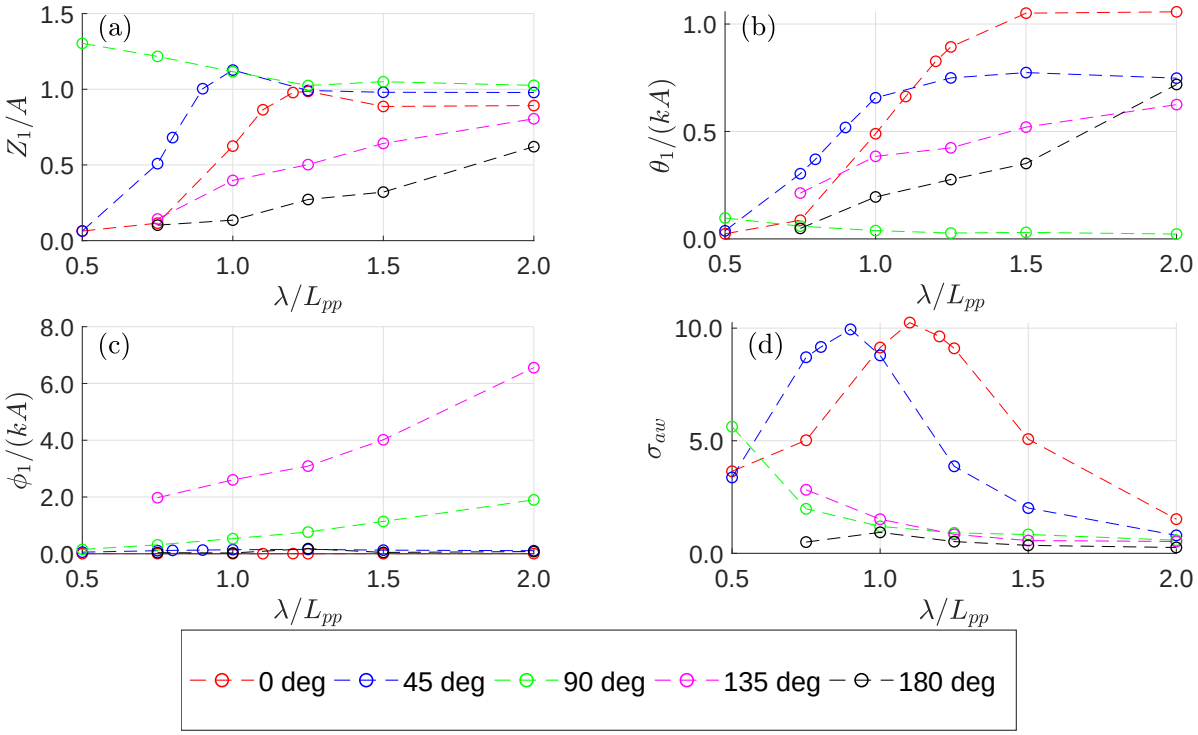

Figure 13: Present CFD results as function of wave heading and non-dimensional wavelength (λ/L_{pp}). (a) Heave, 1st amplitude (Z_1); (b) Pitch, 1st amplitude (θ_1); (c) Roll, 1st amplitude (ϕ_1); (d) Added resistance (σ_{aw}).

and 135 ° headings are increasing, when the wavelength is increased. This is because the encounter frequency is getting close to the natural roll frequency, when the wavelength is increased. The roll responses for the 135 ° heading are larger than for the 90 ° since the encounter frequencies of the studied waves at the 135 ° heading are closer to the natural roll frequency than the studied waves for the 90 ° heading.

Figure 13d shows the added resistance as function of wave heading and non-dimensional wavelength. Compared with the results presented in the previous sections, two extra results for the 0 ° and 45 ° headings are also included to better capture peak values of the added resistance curves. The maximum added resistance for the 90 ° heading is observed for the $\lambda/L_{pp} = 0.5$ wave. As mentioned previously, this wave has an encounter frequency very close to the natural heave and pitch frequencies causing large heave and pitch responses and added resistance at this wave. The maximum added resistance for the studied waves with a heading of 135 ° is found for the $\lambda/L_{pp} = 0.75$ wave, which is the shortest wave studied at this heading. The added resistance for the studied waves at the 180 ° are small, however still positive.

4 CONCLUSION

This study presented a systematic verification and validation of seakeeping responses and added resistance of the KCS container ship in regular oblique waves by using a CFD approach with turbulence modelling. Convergence studies of both the temporal and spatial discretization errors are presented. Discussions are made to determine affordable time steps and mesh sizes while to keep the discretization errors acceptable. The yaw and surge motions are constrained by user-implementations in the commercial software, which consist of additions of springs and concentrated forces/moment to cancel the fluid forces and moments. The mesh and time step convergence studies shows that the sum of the spatial and temporal discretization errors for an affordable calculation is less than 5 %, which is smaller than the average standard deviation of the experiments by (Sanada et al., 2021). A study of

the empty wave tank shows that the wave generation is successful, but causes the loss of incident wave amplitude due to numerical diffusion of less than 4 % for most test cases. 28 test cases are studied with different combinations of wave heading and wavelength. For each test case, the added resistance as well as the heave, pitch, and roll response are compared with previously reported potential flow and CFD results and up to three sets of experimental data. Due to the loss of incident wave amplitude caused by numerical diffusion, the motion and added resistance results are non-dimensionalized based on the actual incident wave amplitude obtained from separate runs in empty wave tank, where similar spatial and temporal discretization is used. In most cases the discrepancy between the experiments and the present CFD results are within the uncertainty of the experiments. In some cases, especially at 135 ° and 180 ° headings, the experimental uncertainty is significant. If experiments with smaller uncertainties become available, a better validation would be possible. It is found that the present CFD results in general have better agreement with the experiments than what previous reported CFD results had. In general, both the previously reported potential flow results and the present CFD results predicts the motion responses well. However, the added resistance predicted by the present CFD model is in better agreement with the experiments, than the potential flow results are. The tendencies in the results of the present CFD model matches very well the expected behaviour regarding the natural motion frequencies of the ship.

ACKNOWLEDGEMENT

The research is supported by the Danish Maritime Fund under grant 2018-11, whose support is greatly appreciated.

REFERENCES

Bunnik, T. H. J. (1999). *Seakeeping calculations for ships, taking into account the non-linear steady waves*. PhD thesis, Delft University of Technology.

Celik, I. B., Ghia, U., Roache, P. J., Freitas, C. J., Coleman, H., and Raad, P. E. (2008). Procedure for estimation and reporting of uncertainty due to discretization in CFD applications. *J. Fluids Engng.*, 130:078001.

Chuang, Z. and Steen, S. (2013). Speed loss of a vessel sailing in oblique waves. *Ocean Engng.*, 64:88–99.

Faltinsen, O. (1993). *Sea Loads on Ships and Offshore Structures*. Cambridge University Press.

Ferziger, J. H. and Peric, M. (2002). *Computational methods for fluid dynamics*. Cambridge University Press, 3 edition.

Fujii, H. and Takahashi, T. (1975). Experimental study on the resistance increase of a large full ship in regular oblique waves. *J. Soc. Nav. Archit. Japan*, 137:132–137.

Gong, J., Yan, S., Ma, Q., and Li, Y. (2020). Added resistance and seakeeping performance of trimarans in oblique waves. *Ocean Engng.*, 216:1–19.

Hino, T., Stern, F., Larsson, L., Visonneau, M., Hirakata, N., and Kim, J. (2020). *Numerical ship hydrodynamics: An assessment of the Tokyo 2015 workshop*. Springer-Verlag.

Hirt, C. W. and Nichols, B. D. (1981). Volume of fluid (VOF) method for the dynamics of free boundaries. *J. Comput. Phys.*, 39(1):201–225.

Ikeda, Y., Himeno, Y., and Tanaka, N. (1978). Components of roll damping of ship at forward speed. *J. Soc. Nav. Archit. Japan*, 143:113–125.

Irkal, M. A. R., Nallayarasu, S., and Bhattacharyya, S. K. (2019). Effect of forward speed on roll damping of a container ship using URANS simulations. *Lect. Notes Civ. Eng.*, 22:187–201.

Jasak, H., Vukčević, V., Gatin, I., and Lalović, I. (2018). Cfd validation and grid sensitivity studies of full scale ship self propulsion. *Int. J. Nav. Archit. Ocean Eng.*, 11(1):33–43.

Jin, Y., Chai, S., Duffy, J., Chin, C., and Bose, N. (2017). URANS predictions of wave induced loads and motions on ships in regular head and oblique waves at zero forward speed. *J. Fluids Struct.*, 74:178–204.

Kim, M., Hizir, O., Turan, O., Day, S., and Incecik, A. (2017a). Estimation of added resistance and ship speed loss in a seaway. *Ocean Engng.*, 141:465–476.

Kim, M., Hizir, O., Turan, O., and Incecik, A. (2017b). Numerical studies on added resistance and motions of KVLCC2 in head seas for various ship speeds. *Ocean Engng.*, 140(May):466–476.

Kim, Y., Kim, K.-H., Kim, J.-H., Kim, T., Seo, M.-G., and Kim, Y. (2011). Time-domain analysis of nonlinear motion responses and structural loads on ships and offshore structures: development of WISH programs. *Int. J. Nav. Archit. Ocean Eng.*, 3(1):37–52.

Liu, C., Wang, J., and Wan, D. (2018). CFD computation of wave forces and motions of DTC ship in oblique waves. *J. Offshore Pol. Eng.*, 28(2):154–163.

Liu, S. and Papanikolaou, A. (2016). Prediction of the added resistance of ships in oblique seas. In *Proceedings of the International Offshore and Polar Engineering Conference*, pages 495–502.

Mikkelsen, H., Steffensen, M. L., Ciortan, C., and Walther, J. H. (2019). Ship scale validation of CFD model of self-propelled ship. In *MARINE 2019 Computational Methods in Marine Engineering VIII*, pages 718–729.

Mikkelsen, H. and Walther, J. H. (2020). Effect of roughness in full-scale validation of a CFD model of self-propelled ships. *Appl. Ocean Research*, 99:102162.

Molland, A., Turnock, S., and Hudson, D. (2011). *Ship resistance and propulsion*. Cambridge University Press.

Mousavi, S. M., Khoogar, A. R., and Ghasemi, H. (2020). Time domain simulation of ship motion in irregular oblique waves. *J. Appl. Fluid Mech.*, 13(2):549–559.

Muzaferija, S. and Perić, M. (1997). Computation of free-surface flows using the finite-volume method and moving grids. *Num. Heat Trans., B*, 32(4):369–384.

Niklas, K. and Pruszko, H. (2019). Full-scale CFD simulations for the determination of ship resistance as a rational, alternative method to towing tank experiments. *Ocean Engng.*, 190:1–13.

Ohmori, T. (1998). Finite-volume simulation of flows about a ship in maneuvering motion. *J. Mar. Sci. Tech.*, 3(2):82–93.

Park, D. M., Kim, Y., Seo, M. G., and Lee, J. (2016). Study on added resistance of a tanker in head waves at different drafts. *Ocean Engng.*, 111:569–581.

Park, D.-M., Lee, J.-H., Jung, Y.-W., Lee, J., Kim, Y., and Gerhardt, F. (2019). Experimental and numerical studies on added resistance of ship in oblique sea conditions. *Ocean Engng.*, 186:106070.

Psaraftis, H. N. and Kontovas, C. A. (2014). Ship speed optimization: Concepts, models and combined speed-routing scenarios. *Transp. Res. Part C Emerg. Technol.*, 44:52–69.

Richardson, L. F. (1910). The approximate arithmetical solution by finite differences of physical problems involving differential equations, with an application to the stresses in a masonry dam. *Phil. Trans. R. Soc. A*, 210:307–357.

Richardson, L. F. and Gaunt, J. A. (1927). The deferred approach to the limit. Part I. Single lattice. Part II. Interpenetrating lattices. *Phil. Trans. R. Soc. A*, 226:299–361.

Roache, P. J. (1998). Verification of codes and calculations. *AIAA J.*, 36(5):696–702.

Sadat-Hosseini, H., Toxopeus, S., Kim, D. H., Sanada, Y., Stocker, M., Otzen, J. F., Toda, Y., and Stern, F. (2015). Experiments and computations for KCS added resistance for variable heading. In *5th World Maritime Technology Conference*, pages 1–15.

Sadat-Hosseini, H., Wu, P. C., Carrica, P. M., Kim, H., Toda, Y., and Stern, F. (2013). CFD verification and validation of added resistance and motions of KVLCC2 with fixed and free surge in short and long head waves. *Ocean Engng.*, 59:240–273.

Salvesen, N., Tuck, E., and Faltinsen, O. (1970). Ship motions and sea loads. *Trans. - Soc. Nav. Archit. Mar. Eng.*, 78:250–287.

Sanada, Y., Simonsen, C., Otzen, J., Sadat-Hosseini, H., Toda, Y., and Stern, F. (2021). *Experimental data for KCS added resistance and ONRT free running course keeping/speed loss in head and oblique waves*, volume 94. Springer-Verlag.

Shih, T.-H., Liou, W. W., Shabbir, A., Yang, Z., and Zhu, J. (1995). A new k-ϵ eddy viscosity model for high Reynolds number turbulent flows. *Computers & Fluids*, 24(3):227–238.

Siemens (2020). STAR-CCM+ user guide, version 2020.1.

Simonsen, C. D., Otzen, J. F., Joncquez, S., and Stern, F. (2013). EFD and CFD for KCS heaving and pitching in regular head waves. *J. Mar. Sci. Tech.*, 18:435–459.

Sprenger, F., Hassani, V., Maron, A., Delefortrie, G., Zwijnsvoorde, T. V., Cura-Hochbaum, A., and Lengwinat, A. (2016). Establishment of a validation and benchmark database for the assessment of ship operation in adverse conditions. In *35th International Conference on Ocean, Offshore and Arctic Engineering*, pages 1–12.

Storm-Tejsen, J., Yeh, H. Y. H., and Moran, D. D. (1973). Added resistance in waves. *Trans. - Soc. Nav. Archit. Mar. Eng.*, 81:250–279.

Uharek, S. and Cura-Hochbaum, A. (2018). The influence of inertial effects on the mean forces and moments on a ship sailing in oblique waves Part B: Numerical prediction using a RANS code. *Ocean Engng.*, 165:264–276.

Valanto, P. and Hong, Y. P. (2015). Experimental investigation on ship wave added resistance in regular head, oblique, beam, and following waves. In *Proceedings of the International Offshore and Polar Engineering Conference*, pages 19–26.

Vukcevic, V. and Jasak, H. (2016). Validation and verification of decomposition model based on embedded free surface method for oblique wave seakeeping simulations. In *Tokyo 2015: A Workshop on CFD in Ship Hydrodynamics*, pages 495–502.

Wilcox, D. C. (1998). *Turbulence modeling for CFD*. DWC Industries, 2 edition.

Wu, P.-C., Hossain, M. A., Kawakami, N., Tamaki, K., Kyaw, H. A., Matsumoto, A., and Toda, Y. (2020). EFD and CFD study of forces, ship motions, and flow field for KRISO container chip model in waves. *J. Ship. Res.*, 64(1):61–80.

Yang, Y., Zhu, R., and Hong, L. (2019). A frequency-domain hybrid HOBEM for motion responses and added resistance of ships sailing in head and oblique waves. *Ocean Engng.*, 194:106637.